

Noise2Ghost: Self-supervised deep convolutional reconstruction for ghost imaging

Mathieu Manni, Dmitry Karpov , K. Joost Batenburg , Sharon Schwartz , Nicola Viganò 

Abstract—We present a new self-supervised deep-learning-based Ghost Imaging (GI) reconstruction method, which provides unparalleled reconstruction performance for noisy acquisitions among unsupervised methods. We present the supporting mathematical framework and results from theoretical and real data use cases. Self-supervision removes the need for clean reference data while offering strong noise reduction. This provides the necessary tools for addressing signal-to-noise ratio concerns for GI acquisitions in emerging and cutting-edge low-light GI scenarios. Notable examples include micro- and nano-scale x-ray emission imaging, e.g., x-ray fluorescence imaging of dose-sensitive samples. Their applications include in-vivo and in-operando case studies for biological samples and batteries.

Index Terms—Ghost imaging, deep learning, image reconstruction, inverse problems, reconstruction algorithms.

I. INTRODUCTION

Ghost imaging (GI) is a paradigm-changing technique that is mostly known and anticipated for its promise to cut radiation doses. However, these possible radiation dose advantages rely on a much more fundamental concept: The ability to choose the trade-off between spatial resolution, field-of-view (FoV), and acquisition time somewhat independently of the incident beam size. Traditionally, to spatially resolve diffused signals like x-ray fluorescence (XRF), one had to raster scan the object of interest with focused illumination (pencil-beam, PB, Fig. 1a). The PB focal spot size determines the spatial resolution. GI achieves that by probing extended regions of a sample at once with structured illumination (Fig. 1b). This provides spatially resolved information, whose resolution is independent of the beam size and detector pixel size, but depends instead on the size of the beam structures.

A detector that does not observe the illumination beam collects the signals of interest. The acquired GI realizations, composed of the detected signals with each associated illumination beam structure, are then combined and computationally reconstructed into a two-dimensional projection image of the probed object (in the given contrast). This means that the acquired

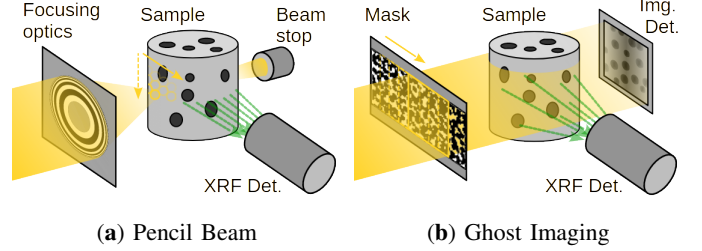


Fig. 1: Schematic representation of diffused emission signal acquisitions (e.g., x-ray fluorescence imaging) using pencil raster beam scanning (a) and ghost imaging (b). The former uses a point beam to scan every pixel to form an image, while the latter illuminates the sample with a series of structured beams.

data mathematically resides in a different space from the reconstructed image space, and the reconstruction problem is a so-called *inverse problem*. The algorithm used to perform this inversion, known as the *reconstruction method*, significantly influences the quality and accuracy of the reconstructed image, particularly under noisy conditions. GI is independent of the contrast and probe type used, and it has been demonstrated with radiation across the whole electromagnetic spectrum [1], [2], neutrons [3], electrons [4], and atoms [5]. Thus, it can be used for the same applications where PB raster scanning is used.

The advantages of GI compared to PB acquisitions stem from the inherent small- and large-scale correlations found in natural images, which make them compressible under suitable representations [6], while non-structured noise is not. Thanks to the structured illumination, which can capture unique large- and small-scale information for each measurement, GI grants image reconstruction with fewer data points than reconstructed pixels. Thus, GI unlocks potential gains in acquisition speed or deposited dose, compared to raster scanning, by simply reducing the number of acquired data points [7].

GI offers a specific advantage over PB scanning for dose-sensitive samples. High-flux focused PBs create significant excess charges in small localized regions at each exposure from radiation-induced local ionization of the samples. This is one of the main contributors to damage in biological samples and the skewing of functioning parameters in batteries during acquisitions. On the contrary, GI creates this same charge on a much larger area (i.e., the whole illumination field-of-view). The latter can recombine and/or disperse faster than the former, leading to lower degradation over time. For instance, in cryogenic electron microscopy (also known as cryo-EM),

M. Manni was with the ESRF — The European Synchrotron, Grenoble, 38000, France, and with the Physics Department and Institute of Nanotechnology and Advanced Materials, Bar Ilan University, Ramat Gan, 52900, Israel (e-mail: mathieu.manni@esrf.fr).

D. Karpov is with the Université Grenoble Alpes, Pôle PEM, CEA, MEM, Grenoble, 38000, France (e-mail: dmitry.karpov@univ-grenoble-alpes.fr).

K. J. Batenburg is with the Leiden Institute of Advanced Computer Science, Leiden Universiteit, 2333, CA Leiden, The Netherlands (e-mail: k.j.batenburg@liacs.leidenuniv.nl).

S. Schwartz is with the Physics Department and Institute of Nanotechnology and Advanced Materials, Bar Ilan University, Ramat Gan, 52900, Israel (e-mail: sharon.schwartz@biu.ac.il).

N. Viganò is with the Université Grenoble Alpes, CEA, IRIG-MEM, Grenoble, 38000, France (e-mail: nicola.vigano@cea.fr).

Manuscript received XXX; revised XXX.

reduced dose rates have been observed to produce less damage compared to higher dose rates at the same total dose [8].

Thanks to all these advantages, GI has the potential to spark many breakthroughs in applications in various fields ranging from biomedical imaging to remote sensing. However, GI has only seen limited applicability so far, especially in the above-mentioned nano-scale imaging applications. In these cases, the observed signals are affected by overwhelmingly high Poisson noise levels due to their very small photon fluxes. This noise type does not enjoy the intrinsic noise reduction of GI, known as Felgett's advantage, thus reducing GI's advantage over PB [7]. Here, we propose a GI reconstruction method particularly suited for working with acquisitions affected by high noise levels, regardless of whether the noise type is Gaussian or Poisson. Our method leverages the latest developments in unsupervised machine learning (ML) techniques, so it does not require high-quality reference data. This work is a step towards practical applications of GI, particularly for photon-limited scenarios like nano-scale emission imaging.

II. METHOD

In this section, we present the proposed method Noise2Ghost (N2G). First, we introduce related methods. Then, we describe the signal formation (forward) model and present our proposed reconstruction method. Finally, we show how this method addresses random acquisition noise.

A. Existing methods

GI's ability to obtain images with more pixels than the acquired realizations means that the associated reconstruction problem is undersampled. These undersampled reconstructions require some prior knowledge (regularization) to recover an accurate image: Unregularized least-squares (LS) reconstructions present specific high-frequency large-scale artifacts that resemble high noise levels. Methods employing convolutional neural networks (CNNs) are currently the best-performing tools for image processing applications. They can capture small- and large-scale correlations and learn the most suitable representations to capture the features present in the treated signals (acting like regularizers) [9]. Thus, they are also better suited for GI reconstructions than traditional variational methods, e.g., Total Variation (TV) minimization, which use strong but also rather simple *a priori* assumptions on the types of features present in the reconstructed images.

ML methods and CNN architectures have both seen an explosion in development and applications over the last decade. Quite a few ML methods have been specifically developed for GI reconstructions. Notable examples are supervised methods [10], where a CNN (e.g., a U-net [11]) compares examples of LS GI reconstructions from highly undersampled acquisitions against their corresponding high-quality reconstructions. The network learns to identify the corrupted features in the LS images and to replace them with their expected shape. This approach is heavily dependent on large amounts of known examples that present strong similarity to the images of interest. It also requires specific training data for each acquisition parameter variation (e.g., noise levels, image size, levels of undersampling, etc).

Untrained generator-network methods do not require pre-training of the model against reference high-quality images, removing the need for large databases of reference images [12], [13]. They can incorporate the knowledge of the image formation model in the learning algorithm (an approach of physics-informed ML), and make the trained model learn to produce an image that fits the acquired data. A good example is the method called GIDC [14], which is based on the deep image prior (DIP) [9]. As a drawback, these methods exhibit lower reconstruction quality for high noise levels in the acquired data. They delegate noise reduction solely to regularization and early stopping. Similar to DIP-based methods, implicit neural representations (INRs) -based methods use untrained NNs to reconstruct an image without high-quality reference data [15], [16]. INR-based methods use multi-layer perceptron (MLP) NNs and accept pixel coordinates instead of input images. During the training, the MLP learns a representation of the imaged object, which produces the desired image for the input coordinates.

Self-supervised methods like Noise2Noise (N2N) use the same training procedure as the supervised methods, but they use noisy images as targets [17]. They only require two noisy realizations of the same measurement (e.g., two noisy images of the same scene) and exploit the fact that the only difference between the two measurements should be the noise. Thus, given one of the two measurements, they train the CNN to predict the other and vice versa. As previously mentioned, CNNs can capture small and large-scale correlations, leading them to learn the features of the measurements while discarding their uncorrelated parts, i.e., the noise. N2N can be adapted to work with inverse problems like computed tomography [18]. However, as we will also see in section II-E, it does not handle the so-called *missing realization* problem, which refers to artifacts arising from not having enough realizations to represent the imaged objects, and that is usually an important source of noise in GI reconstructions.

B. Forward model and variational methods

Here, we provide the mathematical description of the signal formation and the deep image prior (DIP) reconstruction, which will serve as a basis for our method's derivation. Let us represent the discretized expected image of the studied object as the vector $x^* \in \mathbb{R}^N$, where N is the number of its pixels. We probe x^* with a set of structured illumination patterns $\mathcal{W} = \{w_1, w_2, \dots, w_m\}$, which form the acquisition matrix $W = [w_1, w_2, \dots, w_m] \in \mathbb{R}^{M \times N}$, where M is the number of measurements. If we assume that the interaction between the property represented by x^* and the illumination patterns W is linear, then the recorded signal $y \in \mathbb{R}^M$, corrupted by an uncorrelated zero-mean noise ϵ is given by:

$$y = Wx^* + \epsilon = b + \epsilon \quad (1)$$

where $b \in \mathbb{R}^M$ is the non corrupted signal. The reconstruction aims to recover the vector \hat{x} that is the most probable estimate of the clean image x^* . Regularized variational methods seek \hat{x} by solving the following minimization problem:

$$\hat{x} = \underset{x}{\operatorname{argmin}} \frac{1}{2} \|Wx - y\|_2^2 + \lambda R(x) \quad (2)$$

Where $R : \mathbb{R}^N \rightarrow \mathbb{R}$ denotes a regularization term that imposes some *prior knowledge* on the reconstruction. This prior knowledge is often related to the structural properties of the to-be-reconstructed image, and it is supposed to enhance its signal-to-noise ratio. A common choice of regularization is the so-called total variation (TV) minimization, which promotes reconstructed images with sparse gradients. This, in turn, imposes short-range correlations in the reconstructions. Unsupervised generative machine learning methods have taken inspiration from Eq. (2) [12], and developed an image recovery scheme that seeks to solve a very similar minimization problem, but on the output of a machine-learning model (typically a CNN), as follows:

$$\hat{\theta} = \underset{\theta}{\operatorname{argmin}} \frac{1}{2} \|W N_{\theta}(r) - y\|_2^2 + \lambda R(N_{\theta}(r)) \quad (3a)$$

$$\hat{x} = N_{\hat{\theta}}(r) \quad (3b)$$

where $r \in \mathbb{R}^N$ is any input image, which could be randomly chosen, $N_{\theta} : \mathbb{R}^N \rightarrow \mathbb{R}^N$ the model and $\theta \in \mathbb{R}^T$ is its parameters vector with T different parameters. In [14], $r = W^\dagger y$ where W^\dagger is the pseudo-inverse of W , making r the least-squares reconstruction. The model N_{θ} learns to produce the image \hat{x} that satisfies both the forward model Eq. (1) and the regularization R , weighted by the λ parameter. Neural networks have notions of non-locality and non-linearity in their response, which can behave as an additional prior on top of R [9] when the training process is stopped before convergence.

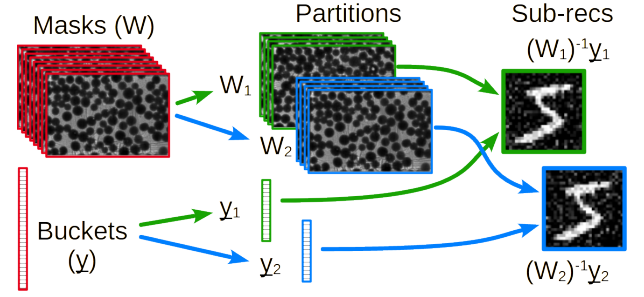
While Eq. (3) has proven to help with the reconstruction of under-determined acquisitions [14], it is not tuned to deal with strong random noise. Following the same derivation steps as in [18], the expected prediction error of the data fitting term in Eq. (3a) is:

$$\begin{aligned} \mathbb{E}_y \|W N_{\theta}(r) - y\|_2^2 \\ = \mathbb{E}_{b, \epsilon} \|W N_{\theta}(W^\dagger(b + \epsilon)) - (b + \epsilon)\|_2^2 \end{aligned} \quad (4)$$

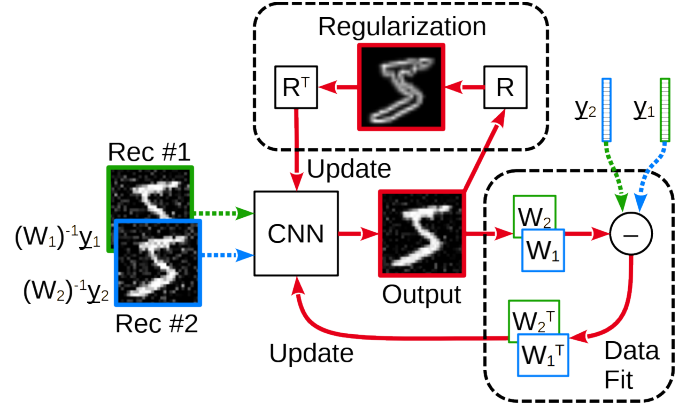
which is intuitively minimized when $N_{\theta} = I$ (the identity matrix). Thus, noise reduction is solely delegated to the regularization term R . Therefore, this reconstruction technique might not be able to provide an advantage over traditional variational methods in this specific scenario.

C. Proposed method: Noise2Ghost (N2G)

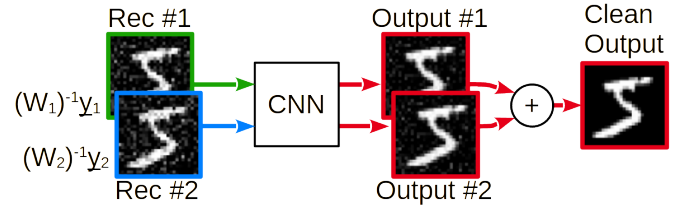
Here, we propose our CNN-based noise-tolerant unsupervised GI reconstruction method. It is inspired by DIP and N2N while addressing their limitations, namely accounting for the random noise in the optimization technique and the missing realization artifacts, respectively. We start from the assumption that by selecting a subset of the original realization set (i.e., the collection of all the acquired signals paired with the corresponding illumination patterns), we should obtain a degraded reconstruction due to a decrease in captured information. However, the degraded reconstruction should still represent the same signal as the reconstruction from the full realization set. This means that if we partition the realizations into subsets with equal numbers of realizations, we should obtain equivalent but different and degraded sub-reconstructions.



(a) Realizations (masks and buckets) partitioning.



(b) Self-supervised model (CNN) training.



(c) Prediction of the final reconstruction.

Fig. 2: Schematic representation of the proposed method: (a) The partitioning of the realizations set, generating the partial reconstructions (sub-recs). (b) The training procedure, which adjusts the model weights to minimize the residual between the projection of each partial prediction against the set of realizations not used for the its corresponding input. (c) The prediction of the final reconstruction obtained from the averaged sub-reconstructions.

We partition the realizations in k splits $k \in [1, K]$, producing K different sub-reconstructions (i.e., a k -tuple of reconstructions). Each sub-reconstruction in the said k -tuple has unique noise characteristics compared to the other reconstructions, and it provides different information on the FoV. From the partitioned data vectors y_k we compute the sub-reconstructions x_k as follows (Fig. 2a):

$$x_k = W_k^\dagger y_k = W_k^\dagger (b_k + \epsilon_k) \quad (5)$$

where W_k^\dagger is pseudo-inverse of the partition forward model W_k , and b_k is the clean data.

Each sub-reconstruction x_k represents the same signal but has a different noise. In N2G, we feed each of these sub-reconstructions to the model, and then we optimize the fol-

lowing minimization problem (Fig. 2b) by comparing them against the realizations that were not used to reconstruct them:

$$\hat{\theta} = \operatorname{argmin}_{\theta} \frac{1}{2} \sum_k \sum_{i \neq k} \|W_i N_{\theta}(x_k) - y_i\|_2^2 + \lambda R(N_{\theta}(x_k)) \quad (6a)$$

$$\hat{x} = \frac{1}{K} \sum_k N_{\hat{\theta}}(x_k). \quad (6b)$$

Since the different sub-reconstructions x_k should represent the same signal, we would like the model to produce the same result for each. Thus, the model should learn to differentiate between the actual signal and random noise. This is in opposition to Eq. (3a), where the same realizations were used for the input reconstruction and as targets in the learning loss. Finally, Fig. 2c represents how Eq. (6b) produces the reconstructed images.

D. Self-supervised random noise reduction

We now derive the noise-reduction properties of Eq. (6a). Reconstruction noise comes from two main sources: Measurement noise; and the lack of information from a low number of realizations, which creates the so-called *missing realization* artifacts. These noise sources can be represented in the sub-reconstructions x_k as follows:

$$x_k = x + v_k + W_k^{\dagger} \epsilon_k = x + v_k + t_k \quad (7a)$$

$$W_k v_k = 0 \quad (7b)$$

$$W_k x_k = y_k + \epsilon_k \quad (7c)$$

where $W_k^{\dagger} \epsilon_k = t_k$ is the pseudo-inverse of the bucket measurement noise, while the vector $v_k \subseteq \ker W_k$ describes spurious solutions that could be added to the reconstruction, and still fit the data. Our method focuses on the random measurement noise, and the desired noise reduction effect is given by the specific construct of the data fitting term from Eq. (6a). When projecting the predicted image onto the target data from the other splits, the projected noise from the k th split will be inconsistent with the random noise from the other $K-1$ splits. This can be seen by substituting Eq. (7a) and Eq. (5) into the data fitting term of Eq. (6a):

$$\frac{1}{2} \sum_{i \neq k} \|W_i N_{\theta}(x + v_k + W_k^{\dagger} \epsilon_k) - (b + \epsilon_i)\|_2^2 \quad (8)$$

As ϵ_k is independent of any other ϵ_i and their domains do not overlap (Appendix A from [19]), the expected prediction error of Eq. (8) becomes:

$$\mathbb{E}_{b, \epsilon, i \neq k} \|W_i N_{\theta}(x + v_k + W_k^{\dagger} \epsilon_k) - b_i\|_2^2 + \mathbb{E}_{b, \epsilon, i \neq k} \|b_i - (b_i - \epsilon_i)\|_2^2. \quad (9)$$

This can be further simplified into:

$$\mathbb{E}_{b, i \neq k} \|W_i N_{\theta}(x_k) - b_i\|_2^2 + \mathbb{E}_{\epsilon, i \neq k} \|\epsilon_i\|_2^2 \quad (10)$$

where the term $\|W_i N_{\theta}(x_k) - b_i\|_2^2$ is the *supervised reconstruction error*, and the term $\|\epsilon_i\|_2^2$ is the signal noise variance. In the supervised reconstruction term, the acquisition noise is not present. This means that it is equivalent to having noiseless

realizations as the targets of our N2G reconstruction, thus providing the noise suppression characteristics of Noise2Ghost. The signal noise variance is just a constant in the objective function, which only depends on the acquisition noise and should not contribute to the objective function gradient. In reality, it may introduce some noise in the optimization gradients at very high noise levels. This could interfere with the reconstruction, guiding it towards local minima.

E. Relationship with Noise2Inverse

The Noise2Inverse method addresses the problem in Eq. (6) directly in the reconstruction domain [19], by solving the following problem:

$$\hat{\theta} = \operatorname{argmin}_{\theta} \frac{1}{2} \sum_k \|N_{\theta}(x_k) - \frac{1}{K-1} \sum_{i \neq k} (x_i)\|_2^2 \quad (11a)$$

$$\hat{x} = \frac{1}{K} \sum_k N_{\hat{\theta}}(x_k). \quad (11b)$$

where $x_i = W_i^{\dagger} y_i$ is the pseudo-inverse (LS reconstruction) of the partial set of masks W_i and corresponding buckets y_i with $i \in [1, K]$. Theoretical grounds support this formulation, and it should retrieve the same result as Eq. (6), regarding its noise reduction aspect. However, it does not address the missing realization artifacts and suffers from strong technical limitations. In ghost imaging, artifacts arising from both missing realization noise and random noise are structured and have long-range correlations, i.e., they generally cover the whole FoV. Commonly used models like CNNs have a limited receptive field (i.e., the region around each pixel that the CNN probes and that provides the context for the said pixel) that may not extend to the entire FoV. Depending on the model, this could have a strong negative impact on the denoising performance.

More precisely, about the missing realization artifacts, in [19] it is stated that Eq. (11) would be unable to cope with them. The LS sub-reconstructions cope with the missing realizations by acting as if their bucket values were set to 0. This fixes one given solution v_k for each x_k , out of the infinite solutions that satisfy Eq. (1). This specific choice of v_k is likely incorrect, but it is used as the model learning target in Eq. (11). The formulation we propose in (Eq. (6)) circumvents this limitation by using the measured buckets as “target”, and by leaving the freedom to the model to find a solution that satisfies the forward model in Eq. (1) in the reconstruction space.

A possible approach to overcome the just-discussed limitations of Eq. (11) would be to use variational methods (like in Eq. (2)) to compute the sub-reconstructions. These non-linear methods are known to remove or strongly reduce these long-range artifacts. However, as discussed in [19], their non-linear nature contrasts with the assumptions of Eq. (11). This may then result in a degraded reconstruction quality.

F. Data augmentation

Thanks to the assumption that any permutation (reordering) of the acquired realizations provides the same reconstruction, we can achieve simple and effective data augmentation: We can increase the number of training examples for the self-

supervised method from the measured data. We permute our dataset in p arrangements with $p \in [1, P]$ and partition each arrangement in k splits $k \in [1, K]$, producing KP different sub-reconstructions (i.e., P k -tuples of reconstructions). In practice, the permutations P provide unique mixtures of missing realization artifacts and random noise, while the K splits are still the underlying mechanism for noise reduction. This modifies Eq. (6) into:

$$\hat{\theta} = \underset{\theta}{\operatorname{argmin}} \frac{1}{2} \sum_{p,k} \|W N_{\theta}(x_{p,k}) - y\|_2^2 + \lambda R(N_{\theta}(x_{p,k})) \quad (12a)$$

$$\hat{x} = \frac{1}{PK} \sum_{p,k} N_{\hat{\theta}}(x_{p,k}). \quad (12b)$$

G. Models

We briefly discuss the machine learning models, in particular neural networks (NN), that N2G could leverage. The model should accept multiple images of the same object as input. This is incompatible with INRs, which learn coordinate-based representations of the signal and thus take coordinates as inputs. CNNs and other MLP-based NNs are instead good candidates. Both NN types take images as input and can learn short- and long-range pixel correlations. Thus, N2G is not tied to a specific NN architecture and can take advantage of future developments in that area. MLP-based NNs examples include the Visual Transformer (ViT) [20] and the swin-transformer [21]. CNNs examples include U-Net [11], DnCNN [22], and MS-D net [23]. Regarding the model size, one should try to work with small NNs to minimize the computation time and resources and to limit overfitting. For instance, we suggest models with parameter numbers in the order of 100k for a 100×100 pixels image. However, some models like MS-D net could achieve similar results with 10-20k parameters for similar image sizes. In our tests, we had the best results with U-Net and DnCNN with around 100-300k parameters. Further details will be provided with the results.

III. RESULTS

We now analyze N2G's performance against existing unsupervised methods for reconstructing both synthetic and real data. The reference methods are LS, TV, the GIDC algorithm from [14] (based on DIP), and INRs. For the synthetic test cases, we first derive a method to modulate the noise and compare different noise levels.

A. Synthetic data generation & quantification

We first evaluate the performance of the proposed method on synthetic data, as it provides the ground truth and precisely allows us to control the noise added to the data. We extracted a 100×100 pixels image to be our ground truth (phantom, e.g., from Figs. 5f and 6f) from [24], a curated collection of chromosome images. We generated synthetic random masks with a normalized half-Gaussian distribution and forward projected the phantom to create the corresponding buckets. As discussed in appendix B, we added Poisson noise to the buckets by first multiplying them by the maximum expected emitted number of photons per pixel. We fed the

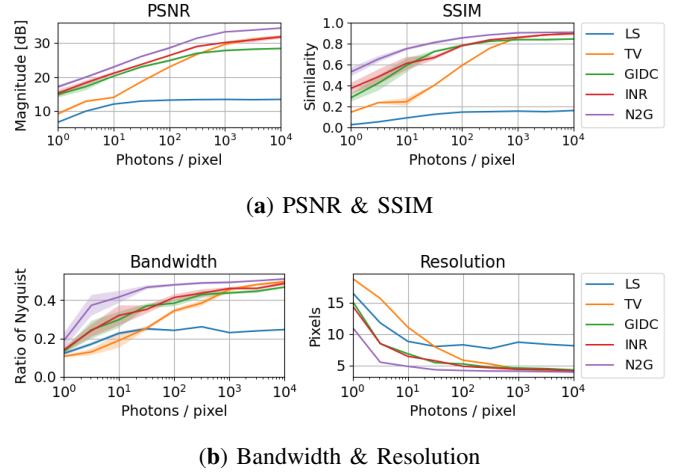


Fig. 3: Synthetic data GI reconstructions of the chromosomes phantom, with $5 \times$ compression ratio, and varying noise levels. The reconstruction algorithm performance is compared for maximum emitted photons per pixel per realization intensities in the range of $[10^0, 10^4]$: (a) reconstruction peak signal-to-noise ratio (PSNR) and structural similarity index (SSIM) against the ground truth, where higher values indicate higher reconstruction quality; and (b) computed bandwidths in terms of the Nyquist frequency and corresponding resolutions in pixels of the images.

resulting mean expected photons per realizations to the Poisson distribution function. We then normalized the signals by dividing the noisy buckets by the same number of expected photons, resulting in signals:

$$y_m = \mathcal{P} \left(C \sum_n w_{mn} x_n \right) / C. \quad (13)$$

We use the constant C to modulate the noise and evaluate its effect on the reconstruction performance of the proposed method.

We evaluate the reconstruction algorithms both visually and with multiple objective metrics: the mean square error (MSE), the peak signal-to-noise ratio (PSNR), the structural similarity index (SSIM), and the resolution, which is estimated from the Fourier ring correlation (FRC). Their formulas are provided in appendix A, while here we shortly describe their meaning. The MSE evaluates the average pixel-wise difference between the phantom and the reconstruction intensity values. The SSIM calculates the similarity between these two images by comparing the inter-dependencies of spatially neighboring pixels over various window sizes [25]. PSNR is based on MSE, but it focuses on the peak intensity power instead of its average. Finally, the FRC computes the similarity in Fourier space between the phantom and the reconstruction for all the sampled frequencies. We estimate the resolution of the reconstruction by finding the intersection of the resulting curve with the threshold function defined in [26].

B. Synthetic data reconstructions across various noise levels

We present three different study cases: In the first case (Fig. 3), we present the performance of the above-mentioned different algorithms (LS, TV, GIDC, INR, and N2G) across

multiple noise levels (i.e. photons per pixel) using only 2000 realizations, corresponding to 20% of the total number of pixels. The simulated maximum emitted photons per pixel per realization (i.e. constant C) intensities span the range of $[10^0, 10^4]$. For each noise level, we generated five different sets of realizations. The same evaluation metrics (e.g. mean error against the phantom, etc) are independently computed for each of the five reconstructions. The presented results indicate the average and standard deviation of the computed metrics. For the TV, GIDC, INR, and N2G reconstructions, the regularization term λ was chosen by cross-validation, by putting aside a set of realizations (10% of the total) and using them to assess the best value over a wide range [27]. For TV, we use a $\lambda \in [10^{-5}, 10^{-1}]$, while for GIDC, INR, and N2G we used a $\lambda \in [10^{-7}, 10^{-4}]$. To improve the procedure's robustness, we ran it three times with different cross-validation sets for each run and averaged the cross-validation loss values between those different runs. For the INR reconstructions, we used a 3-layer feed-forward NN with 512 neurons per layer, sinusoidal activation functions [15], and 64 Fourier embeddings [28]. Regarding specifically GIDC and N2G, we used a U-net [11] with 24 features and 3 decomposition levels ($\sim 276k$ parameters). We fitted the U-net weights with 3000 epochs of the Adam optimizer [29] with a learning rate of 2×10^{-4} and weight decay of 1×10^{-2} . We selected the model weights of the epoch where the cross-validation loss function is minimized. For N2G, we used 4 partitions and 6 permutations ($K = 4$, and $P = 6$).

On the left side of Fig. 3a, we present the peak signal-to-noise ratio (PSNR) of the reconstructions against the phantom. It is evident that N2G consistently achieves superior reconstructions, with PSNRs surpassing those of competing methods by 1–2 dB, highlighting its robustness across diverse imaging conditions. Nonetheless, its advantage seems to diminish under low-photon scenarios. While counterintuitive, this is easily explained by the fact that the lower frequencies are less affected by Poisson noise. PSNR takes all frequencies into account, resulting in a bias towards lower frequencies with low-photon counts. The SSIM, by construction, is instead less affected by lower frequencies. For this reason, on the right side of Fig. 3a, we see that N2G has a growing lead in SSIM for lower photon counts. We also observe that for high photon numbers (equating to low noise), the compression ratio becomes the limiting factor for reconstruction accuracy, and both PSNR and SSIM reach a plateau. From Fig. 3b, we have instead a perspective on how the resolution is degraded with increasing noise levels. We observe that N2G better preserves the reconstruction resolution, by showing a drop-off at lower photon counts than other methods.

Finally, we explore dose considerations by comparing GI with PB and assess N2G's performance against LS, TV, GIDC, and INR. In particular, we evaluate the total sample and average maximum pixel dose necessary to achieve a GI image with PSNR or SSIM quality comparable to a PB scan. From figure Fig. 4a, we observe that in terms of the total dose, PB always outperforms GI at the chosen compression ratio, regardless of the method used, although N2G narrows the difference. Concerning the average maximum pixel dose per exposure

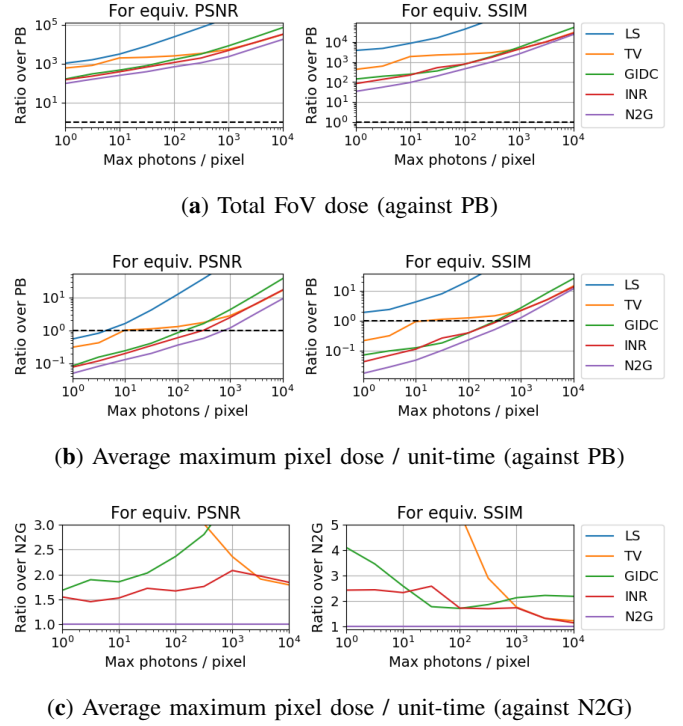
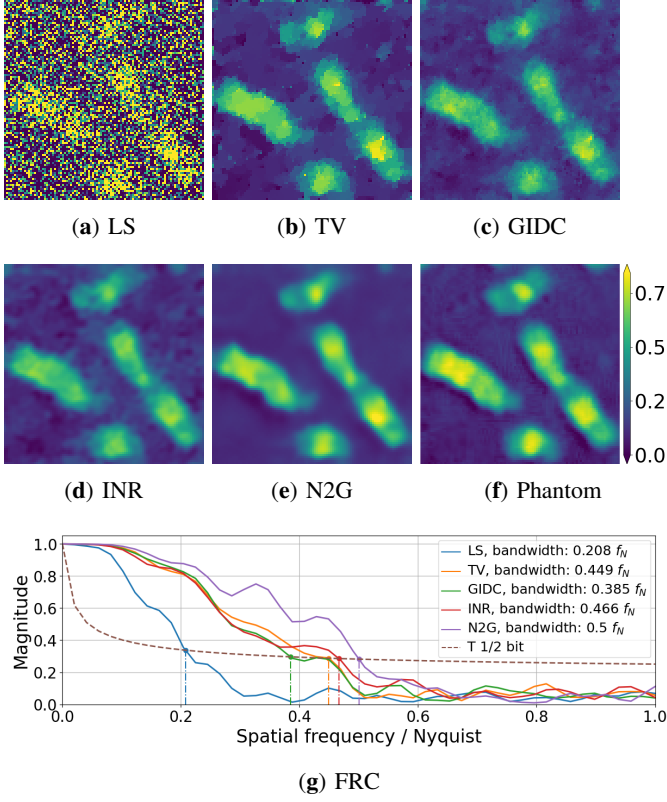


Fig. 4: Dose requirements for the chromosomes phantom, with $5\times$ compression ratio, and varying noise levels. The reconstruction algorithms performance is compared against PB, for maximum emitted photons per pixel per realization intensities in the range of $[10^0, 10^4]$: (a) total required dose for each algorithm to obtain equivalent PSNR and SSIM as a PB acquisition; (b) same plot as (a) for the average maximum pixel dose per illumination; and (c) for N2G.

(Fig. 4b), GI generally exceeds PB's performance when the main noise source is detection noise (except when LS is used). However, N2G still decreases dose requirements compared to the other GI reconstruction techniques and widens the region where GI is preferable over PB. Figure 4c clearly shows this trend by plotting the required dose ratio from LS, TV, GIDC, and INR to obtain the same performance as N2G.

C. In-depth analysis of noisy reconstructions

We now provide an in-depth analysis of two examples: (a) high compression ratio and moderate noise and (b) low compression ratio and very high noise (higher than signal). We present the results for (a) in Fig. 5. We produced 1000 realizations, resulting in a $10\times$ compression ratio. The applied Poisson noise of 10^2 maximum emitted photons per pixel per realization (i.e. constant $C = 10^2$) resulted in fluctuations equal to 24.5% of the mean clean bucket fluctuations. Comparing reconstructions from Figs. 5a to 5e against Fig. 5f, we note that except for the LS reconstruction, all other algorithms, including N2G, can correctly reconstruct the shape of the phantom. The only visible difference is that N2G's reconstruction presents much less high-frequency noise. This results in the N2G reconstruction having the highest resolution (in pixels), PSNR, and SSIM values, and the lowest MSE among all reconstructions. These results are summarized in Fig. 5h.

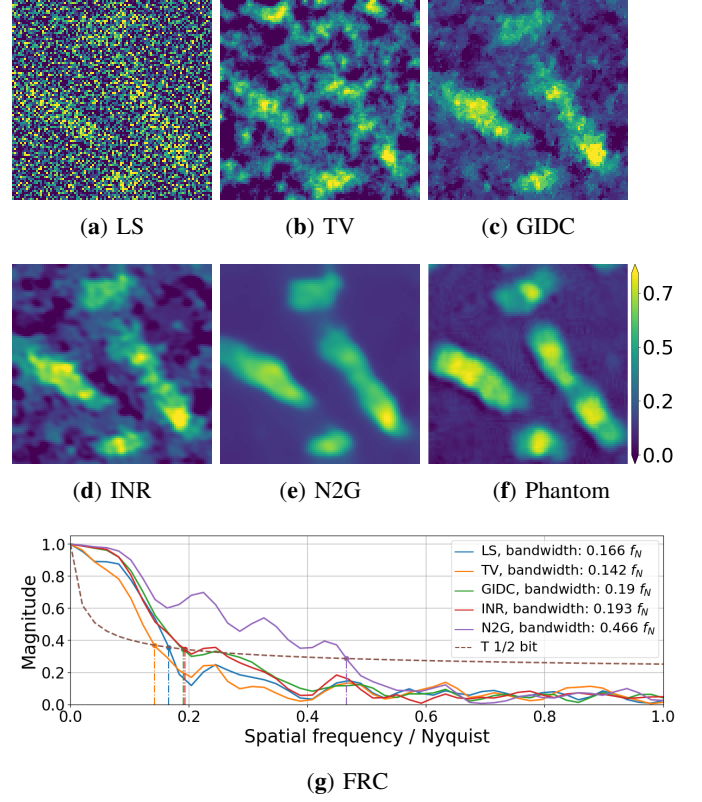


	LS	TV	GIDC	INR	N2G
MSE ↓	0.400	0.004	0.004	0.003	0.001
PSNR ↑	2.50	22.44	22.7	23.27	26.89
SSIM ↑	0.030	0.656	0.672	0.700	0.827
Resolution ↓	9.6	4.4	5.2	4.3	4.0

(h) Performance comparison.

Fig. 5: GI reconstructions of the chromosomes phantom, with $10\times$ compression ratio and moderate Poisson noise: Mean noise fluctuations $\sim 24.5\%$ of the mean clean bucket fluctuations. From (a) to (e) we show the reconstructions of (f) with LS, TV, GIDC, INR and N2G respectively. In (g) and in (h) we present the Fourier ring correlation against (f) and various performance metrics of each reconstruction, respectively.

We present the results of (b) in Fig. 6. Here, we produced 3333 realizations, resulting in a $3\times$ compression ratio. The applied Poisson noise of 2 maximum emitted photons per pixel per realization (i.e. constant $C = 2$) resulted in fluctuations equal to 164.44% of the mean clean bucket fluctuations. All the reconstructed images are noticeably affected by noise with a larger bandwidth than in the previous examples. N2G can suppress high-frequency noise, but cannot completely correct lower-frequency noise. Despite that, by looking at the FRC in Fig. 6g, we notice that it preserves much more bandwidth than the other algorithms and presents a much better resolution. This again results in the N2G reconstruction having the highest PSNR and SSIM values, and the lowest MSE among all reconstructions. These results are summarized in Fig. 6h.



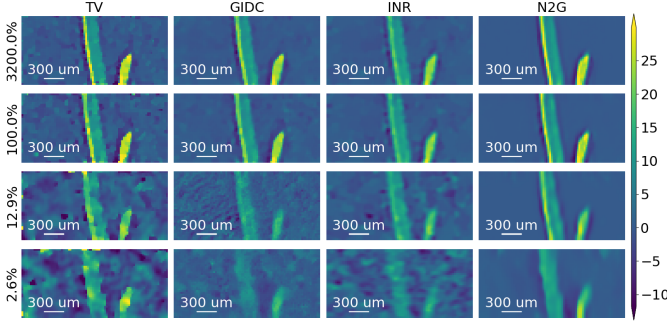
	LS	TV	GIDC	INR	N2G
MSE ↓	0.150	0.047	0.013	0.012	0.006
PSNR ↑	6.74	11.81	17.29	17.79	20.58
SSIM ↑	0.034	0.186	0.336	0.380	0.693
Resolution ↓	12.0	14.2	10.5	10.4	4.3

(h) Performance comparison.

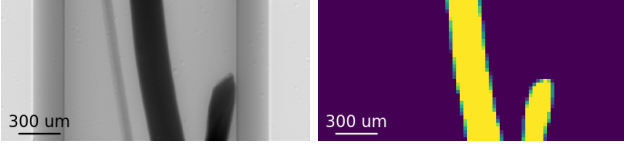
Fig. 6: GI reconstructions of the chromosomes phantom, with $3\times$ compression ratio and very high Poisson noise: Mean noise fluctuations $\sim 164.44\%$ of the mean clean bucket fluctuations. From (a) to (e) we show the reconstructions of (f) with LS, TV, GIDC, INR and N2G respectively. In (g) and in (h) we present the Fourier ring correlation against (f) and various performance metrics of each reconstruction, respectively.

D. X-ray fluorescence data reconstructions

Finally, we compare the reconstruction performance of N2G on real GI data acquired at the beamline ID19 of the ESRF — The European Synchrotron [30]. The considered dataset consists of 42×87 pixels images, with $24\mu\text{m}$ pixel size, and 896 realizations, where the buckets are the emitted XRF signals from a sample composed of a glass capillary and three wires. Two of the three wires are made of Cu, and they will be the focus of this reconstruction. We used the signal from their K_α emission line. At each realization, we exposed the sample to a 26 keV incoming X-ray beam for 0.1 seconds and acquired each realization 32 times. The accumulated 3.2-second exposures serve as high-SNR buckets. Reducing the number of accumulated exposures artificially reduces the collected number of photons (photon flux), thus simulating lower dose depositions. The XRF signals are collected with a single-pixel hyper-spectral detector, whose spectral output



(a) XRF-GI reconstructions of two Cu wires.



(b) Transmission image.

(c) Segmented Cu wires.

	PSNR			SSIM		
	100%	12.9%	2.6%	100%	12.9%	2.6%
TV	30.24	24.34	21.19	0.680	0.319	0.192
GIDC	32.76	23.23	21.51	0.721	0.315	0.217
INR	33.14	24.73	19.43	0.771	0.389	0.182
N2G	35.33	27.75	23.76	0.933	0.796	0.501

(d) PSNR and SSIM of the GI reconstructions.

Fig. 7: Real data GI reconstructions of XRF-GI data from [30], using TV, GIDC, and N2G: (a) presents the reconstructions at different photon counts (and corresponding noise levels); (b) and (c) present an x ray transmission image of the sample at 26 keV and the segmentation of the Cu wires, respectively; and (d) a table of the peak signal-to-noise ratio (PSNR) and structural similarity index (SSIM) of each reconstruction against their high-SNR versions in the top row of (a).

is discretized into 4096 bins of 150 eV energy steps. Each XRF peak has a Lorentzian shape around the mean energy $E_{e,l}$. This means that we observe photon counts in adjacent bins around the expected mean signal energy, which decrease $\sim \gamma_{e,l}/((E_{e,l} - E)^2 + \gamma_{e,l}^2)$ for bins at energy E further away from it, where $\gamma_{e,l}$ is a constant that depends on the emission line. These neighboring bins are either summed or the area under their curve is fitted to increase the signal's SNR. Therefore, we can simulate further dose reductions by summing fewer and lower-count bins.

We present the results of the XRF-GI reconstructions in Fig. 7. Figure 7b presents an X-ray transmission image (radiograph) of the sample, while Fig. 7c indicates the regions that give rise to the XRF signal of interest. As mentioned above, we consider the 0.1-second exposures as the “100% dose” exposures, while the 3.2-second accumulated images serve as ground truth (high-quality reference images). The other two images in Fig. 7a were produced using the five highest-counts and the single highest-counts XRF bins, which provide an average of 12.9% and 2.6% of the reference dose per realization, respectively. These two reduced-flux datasets

could thus correspond to 12.9 ms and 2.6 ms exposures per realization, respectively. The table from Fig. 7d presents the estimated image quality degradation with increasing noise levels, according to PSNR and SSIM. Each result is compared against their own method-related “reference” reconstruction because we lack a PB scan of the object, which would serve as shared ground truth. Despite that, N2G provides the highest noise reduction according to PSNR and SSIM across all the considered reconstruction methods.

IV. CONCLUSIONS & OUTLOOK

In this article, we present a self-supervised deep-learning GI reconstruction method specifically targeted at dealing with random noise in the acquired data. If provided with enough high-quality reference data on the studied samples, existing supervised approaches might exhibit high noise suppression performance, with possibly higher PSNR and/or resolution than our approach. However, gathering high-quality reference data can be expensive and requires extensive and organized efforts, thus sometimes proving to be a difficult or even impossible task. This particularly applies to cutting-edge and niche applications in micro- and nano-imaging, dealing with rare (or even unique) samples with high radiation-dose sensitivity (e.g., biological specimens, battery cells) in in-vivo/in-operando conditions. In those cases, high-quality reference data are usually simply unavailable. Our approach solves this problem with self-supervision, resulting in higher reconstruction performance against the state-of-the-art unsupervised approaches across multiple metrics like MSE, PSNR, SSIM, and image resolution. From both the synthetic test cases and the real data reconstructions, we observe that our method preserves higher reconstruction quality than existing unsupervised methods as the noise increases, i.e., at faster acquisition speeds and/or lower deposited dose, across a suite of case studies. This translates into the following relevant aspects: For the same image quality, we could be looking at a reduction in the acquisition time and/or delivered dose by a factor of $\sim 1.5 - 2$, compared to the best existing unsupervised methods, when working with the lower deposited doses; and the range of deposited doses where GI offers an advantage over PB is also expanded.

The above-mentioned aspects also mean that our method could enable operating GI scans at $\sim 1.5 - 2$ shorter dwell time, resulting in faster GI acquisitions. This aspect is crucial for real case scenarios in two alternative ways: Either increasing acquisition stability or the ability to acquire more realizations for the same dose. In the first case, when paired with the reduced number of GI realizations compared to PB acquisitions, we further reduce the total acquisition times of GI acquisitions, strongly improving the stability of our GI scans. Moreover, compared to PB scans, where the sample moves across the field of view, in a GI acquisition, the sample is fixed [30]. This further consolidates GI as a very attractive technique for reducing sample drifts and positioning errors in nano-scale imaging. Alternatively, the reduced exposure time for each GI realization would also enable more realizations to be acquired per a fixed acquisition time budget. This, in turn, is the only way to reduce the missing-realization noise,

which is the ultimate limit in GI reconstruction quality, as seen earlier in the text.

N2G focuses on noise reduction from the acquired measurements. It delegates dealing with the missing realization artifacts to the generalization power of the underlying model (NN) and the rather simplistic prior knowledge given by the TV term. Future work could tackle this problem with a combination of a few possible approaches, including using stronger or more complex priors than TV (e.g., multi-level undecimated wavelet minimization) and multi-channel/multi-modal information from correlated signals (e.g., the transmission signal in [16]), as demonstrated in computed tomography [31].

APPENDIX

A. Metrics

We give the mathematical definition of the metrics used in section III. For two given signals x_1 and x_2 , MSE, PSNR, and SSIM can be computed as follows:

$$\text{MSE}(x_1, x_2) = \|x_1 - x_2\|_2^2 \quad (14a)$$

$$\text{PSNR}(x_1, x_2) = 20 \log_{10} \|x_1\|_\infty - 10 \log_{10} \text{MSE}(x_1, x_2) \quad (14b)$$

$$\text{SSIM}(x_1, x_2) = \frac{(2\mu_1\mu_2 + c_1)(2\sigma_{12} + c_2)}{(\mu_1^2 + \mu_2^2 + c_1)(\sigma_1^2 + \sigma_2^2 + c_2)} \quad (14c)$$

where $\|x_1\|_\infty = \max(x_1)$, μ and σ are the mean value and the standard deviation respectively of a given signal, the c constants are used to stabilize the fraction, and the SSIM is computed on 7×7 pixel windows. From [26], the FRC is defined as:

$$\text{FRC}_{x_1, x_2}(r_i) = \frac{\sum_{r \in r_i} \mathcal{F}_{x_1}(r) \cdot \mathcal{F}_{x_2}^*(r)}{\sqrt{\sum_{r \in r_i} \mathcal{F}_{x_1}^2(r) \cdot \sum_{r \in r_i} \mathcal{F}_{x_2}^2(r)}} \quad (15)$$

where $\mathcal{F}_x(\cdot)$ is the Fourier transform of a signal x , and $r \in r_i$ is the set of all the pixels at distance r_i from the zero frequency in Fourier space, resulting in $\sum_{r \in r_i}$ being an azimuthal integration at the radius r_i .

B. Derivation of the noise model

Since the proposed method is agnostic of the underlying imaging technique, we first develop an independent evaluation framework from the technique and noise source. We use the guiding example of XRF imaging to derive the just-mentioned generic noise model. For PB acquisitions and a given element e in a compound cmp and the corresponding XRF emission line l , the clean observed signal in the XRF detector is (slightly adapted from Eq. (10) of [32]):

$$\Phi_{e,l}(E_0) = \phi_0(E_0)t\chi_e\sigma_{e,l}(E_0)\rho_{cmp}\nu G_d A_{e,l}(E_0) \quad (16a)$$

$$\nu = p^2\tau \quad (16b)$$

$$G_d = \frac{S_d}{4\pi D_d^2} \quad (16c)$$

$$A_{e,l}(E_0) = \exp \left\{ - \int_{in} \mu(E_0) d\tau - \int_{out} \mu(E_{e,l}) d\tau \right\} \quad (16d)$$

where $\phi_0(E_0)$ is the probing beam's photon flux at the energy E_0 , t the dwell time (exposure time per pixel), ρ_c is the local compound density, χ_e is the local relative concentration of

the said element e in the compound cmp , $\sigma_{e,l}(E_0)$ is the XRF production cross-section, ν is the observed volume, where p is the beam waist (pixel size) and τ the object thickness, G_d is a geometric factor that accounts for the detector surface S_d and distance D_d , and finally $A_{e,l}(E_0)$ is the combined attenuation of the incoming and emitted photons across the sample. The total delivered dose per pixel is $\Phi_0(E_0) = \phi_0(E_0)t$. Equation (16) can be easily modified to account for other emission signals like Compton radiation. The corresponding detected signal is $\Phi_\alpha(E_0)$, where α is the observation angle, is obtained by changing the production cross section $\sigma_{e,l}(E_0)$ to the Compton equivalent, and by removing the elemental concentrations χ_e (as $\sum_e \chi_e = 1$).

The observed signal y on the detector is:

$$y = \mathcal{P}(\Phi_{e,l}(E_0)) + \mathcal{N}_{\mu_d=0, \sigma_d^2} \quad (17)$$

where \mathcal{P} is the photon counting (Poisson – shot) noise of the detection process, and \mathcal{N} is the additive white (Gaussian) noise from the instrument electronics, with mean value $\mu_d = 0$ and a given variance σ_d^2 . Per Eq. (1), $b = \Phi_{e,l}(E_0)$ and $\epsilon = (\mathcal{P}(\Phi_{e,l}(E_0)) - \Phi_{e,l}(E_0)) + \mathcal{N}_{\sigma_d^2}$. In x-ray emission detection, it is safe to assume $\sigma_d^2 = 0$. Thus, we are mostly confronted with Poisson noise, which is mainly modulated by the quantities $\Phi_0(E_0)$, ρ_c , and χ_e .

In XRF imaging, we aim to reconstruct the local relative concentrations χ_e (or actual concentrations $\chi_e\rho_c$), while in Compton imaging, we aim at the compound densities ρ_c . Thus, they correspond to the vector elements x_i from Eq. (1). This means that the other factors in Eq. (16a) can either be considered constant or measured during the acquisitions, and they will contribute as constants in our noise description. Therefore, e.g. for XRF imaging, we can simplify Eqs. (16a) and (17) to account for each measured point j as follows:

$$b_m = \Phi_{e,l,m}(E_0) = \chi_{e,m}c_{e,l}(E_0)\Phi_0(E_0) \quad (18a)$$

$$y_m = \mathcal{P}(\chi_{e,m}c_{e,l}(E_0)\Phi_0(E_0)). \quad (18b)$$

Thus, the noise is modulated by the value of $C = c_{e,l}(E_0)\Phi_0(E_0)$, giving $b = \chi_e C$ and $y = \mathcal{P}(\chi_e C)$. The constant C represents the emitted photons per pixel j for a 100% local element e concentration.

For GI and a homogeneous incoming beam, we modify Eq. (18) as follows:

$$b_m = \Phi_{e,l,m}(E_0) = \sum_n w_{mn} \chi_{e,n} c_{e,l}(E_0) \Phi_0(E_0) \quad (19a)$$

$$y_m = \mathcal{P} \left(\sum_n w_{mn} \chi_{e,n} c_{e,l}(E_0) \Phi_0(E_0) \right) \quad (19b)$$

where w_{mn} are the mask transmission intensities from the projection matrix W in Eq. (1). If $w_{mn} \in [0, 1]$, the constant C represents the maximum emitted photons per pixel. As expected, from Eq. (19) we observe that $W_{PB} = I$, for PB acquisitions. By absorbing the $c_{e,l}(E_0)\Phi_0(E_0)$ into the same constant C as for PB, and normalizing data by C , we obtain Eq. (13).

C. Deposited dose & acquisition time considerations

Equations (18) and (19) offer a way to compare the performance of PB and GI approaches on simulated data, especially

when comparing the respective simulated acquisition time or delivered dose to the sample. For PB acquisitions, we define:

$$\text{Total sample dose: } N\Phi_{0,PB}(E_0) \quad (20a)$$

$$\text{Total pixel dose: } \Phi_{0,PB}(E_0) \quad (20b)$$

$$\text{Max pixel dose / unit-time: } \Phi_{0,PB}(E_0) \quad (20c)$$

while for GI acquisitions:

$$\text{Total sample dose: } \sum_m^M \sum_n^N w_{mn} \Phi_{0,GI}(E_0) \quad (21a)$$

$$\text{Total pixel dose: } \sum_m^M w_{mn} \Phi_{0,GI}(E_0) \quad (21b)$$

$$\text{Max pixel dose / unit-time: } \|w_{\cdot n}\|_{\infty} \Phi_{0,GI}(E_0) \quad (21c)$$

for a given pixel n , where $w_{\cdot n}$ indicates the n -th column of the matrix W . If the matrix elements w_{mn} span $[0, 1]$, then $\sup(W) = 1$ and thus we can assume $\|w_{\cdot n}\|_{\infty} = 1$.

Given the ground truth \hat{x} , a GI reconstruction x_{GI} obtained from synthetic data generated with a value C_{GI} , and a metric $\mathcal{M}(\cdot)$ of choice in the set $\{\text{PSNR}(\hat{x}; \cdot), \text{SSIM}(\hat{x}; \cdot), \dots\}$, we obtain the \hat{C}_{PB} value of a PB acquisition $x_{PB} = y_{PB} = \mathcal{P}(\hat{x}_{C_{PB}})$ that exhibits the closest performance to x_{GI} as:

$$\hat{C}_{PB} = \underset{C_{PB}}{\operatorname{argmin}} \{ \mathcal{M}(x_{GI}) - \mathcal{M}(\mathcal{P}(\hat{x}_{C_{PB}})) \}. \quad (22)$$

Finally, we can compute acquisition time or deposited dose ratios between different techniques, for equivalent image quality, by computing the ratio between the corresponding quantities in Eqs. (20) and (21), with the corresponding C values from Eq. (22).

REFERENCES

- [1] O. Katz, Y. Bromberg, and Y. Silberberg, "Compressive ghost imaging," *Applied Physics Letters*, vol. 95, no. 13, 2009.
- [2] D. Pelliccia, A. Rack, M. Scheel, V. Cantelli, and D. M. Paganin, "Experimental X-Ray Ghost Imaging," *Physical Review Letters*, vol. 117, no. 11, p. 113902, sep 2016.
- [3] A. M. Kingston, G. R. Myers, D. Pelliccia, F. Salvemini, J. J. Bevit, U. Garbe, and D. M. Paganin, "Neutron ghost imaging," *Physical Review A*, vol. 101, no. 5, p. 053844, may 2020.
- [4] S. Li, F. Cropp, K. Kabra, T. J. Lane, G. Wetzstein, P. Musumeci, and D. Ratner, "Electron Ghost Imaging," *Physical Review Letters*, vol. 121, no. 11, p. 114801, sep 2018.
- [5] R. I. Khakimov, B. M. Henson, D. K. Shin, S. S. Hodgman, R. G. Dall, K. G. H. Baldwin, and A. G. Truscott, "Ghost imaging with atoms," *Nature*, vol. 540, no. 7631, pp. 100–103, dec 2016.
- [6] S. L. Brunton and J. N. Kutz, *Data-Driven Science and Engineering*. Cambridge University Press, jan 2019.
- [7] T. J. Lane and D. Ratner, "What are the advantages of ghost imaging? Multiplexing for x-ray and electron imaging," *Optics Express*, vol. 28, no. 5, p. 5898, mar 2020.
- [8] M. Karuppasamy, F. Karimi Nejadasl, M. Vulovic, A. J. Koster, and R. B. G. Ravelli, "Radiation damage in single-particle cryo-electron microscopy: effects of dose and dose rate," *Journal of Synchrotron Radiation*, vol. 18, no. 3, pp. 398–412, may 2011.
- [9] V. Lempitsky, A. Vedaldi, and D. Ulyanov, "Deep Image Prior," in *2018 IEEE/CVF Conference on Computer Vision and Pattern Recognition*. IEEE, jun 2018, pp. 9446–9454.
- [10] S. Rizvi, J. Cao, K. Zhang, and Q. Hao, "DeepGhost: real-time computational ghost imaging via deep learning," *Scientific Reports*, vol. 10, no. 1, p. 11400, jul 2020.
- [11] O. Ronneberger, P. Fischer, and T. Brox, "U-Net: Convolutional Networks for Biomedical Image Segmentation," in *Medical Image Computing and Computer-Assisted Intervention – MICCAI 2015*, 2015, pp. 234–241.
- [12] A. Habring and M. Holler, "Neural-network-based regularization methods for inverse problems in imaging," *GAMM-Mitteilungen*, jul 2024.
- [13] A. Qayyum, I. Ilahi, F. Shamshad, F. Boussaid, M. Bennamoun, and J. Qadir, "Untrained Neural Network Priors for Inverse Imaging Problems: A Survey," *IEEE Transactions on Pattern Analysis and Machine Intelligence*, pp. 1–20, 2022.
- [14] F. Wang, C. Wang, M. Chen, W. Gong, Y. Zhang, S. Han, and G. Situ, "Far-field super-resolution ghost imaging with a deep neural network constraint," *Light: Science & Applications*, vol. 11, no. 1, p. 1, jan 2022.
- [15] V. Sitzmann, J. N. P. Martel, A. W. Bergman, D. B. Lindell, and G. Wetzstein, "Implicit Neural Representations with Periodic Activation Functions," in *Proc. NeurIPS*, 2020.
- [16] J. Li, S. Chen, D. Ratner, T. Blu, P. Pianetta, and Y. Liu, "Nanoscale chemical imaging with structured X-ray illumination," *Proceedings of the National Academy of Sciences*, vol. 120, no. 49, dec 2023.
- [17] J. Lehtinen, J. Munkberg, J. Hasselgren, S. Laine, T. Karras, M. Aittala, and T. Aila, "Noise2Noise: Learning Image Restoration without Clean Data," in *Proceedings of the 35th International Conference on Machine Learning*, ser. Proceedings of Machine Learning Research, J. Dy and A. Krause, Eds., vol. 80. PMLR, 2018, pp. 2965–2974.
- [18] A. A. Hendriksen, D. M. Pelt, W. J. Palenstijn, S. B. Coban, and K. J. Batenburg, "On-the-Fly Machine Learning for Improving Image Resolution in Tomography," *Applied Sciences*, vol. 9, no. 12, p. 2445, jun 2019.
- [19] A. A. Hendriksen, D. M. Pelt, and K. J. Batenburg, "Noise2Inverse: Self-Supervised Deep Convolutional Denoising for Tomography," *IEEE Transactions on Computational Imaging*, vol. 6, pp. 1320–1335, 2020.
- [20] A. Dosovitskiy, L. Beyer, A. Kolesnikov, D. Weissenborn, X. Zhai, T. Unterthiner, M. Dehghani, M. Minderer, G. Heigold, S. Gelly, J. Uszkoreit, and N. Houlsby, "An Image is Worth 16x16 Words: Transformers for Image Recognition at Scale," 2021.
- [21] Z. Liu, Y. Lin, Y. Cao, H. Hu, Y. Wei, Z. Zhang, S. Lin, and B. Guo, "Swin Transformer: Hierarchical Vision Transformer using Shifted Windows," in *2021 IEEE/CVF International Conference on Computer Vision (ICCV)*. IEEE, oct 2021, pp. 9992–10002.
- [22] K. Zhang, W. Zuo, Y. Chen, D. Meng, and L. Zhang, "Beyond a Gaussian Denoiser: Residual Learning of Deep CNN for Image Denoising," *IEEE Transactions on Image Processing*, vol. 26, no. 7, pp. 3142–3155, jul 2017.
- [23] D. M. Pelt and J. A. Sethian, "A mixed-scale dense convolutional neural network for image analysis," *Proceedings of the National Academy of Sciences*, vol. 115, no. 2, pp. 254–259, 2018.
- [24] J.-J. Tseng, C.-H. Lu, J.-Z. Li, H.-Y. Lai, M.-H. Chen, F.-Y. Cheng, and C.-E. Kuo, "An Open Dataset of Annotated Metaphase Cell Images for Chromosome Identification," *Scientific Data*, vol. 10, no. 1, p. 104, feb 2023.
- [25] Z. Wang, A. Bovik, H. Sheikh, and E. Simoncelli, "Image Quality Assessment: From Error Visibility to Structural Similarity," *IEEE Transactions on Image Processing*, vol. 13, no. 4, pp. 600–612, apr 2004.
- [26] M. van Heel and M. Schatz, "Fourier shell correlation threshold criteria," *Journal of Structural Biology*, vol. 151, no. 3, pp. 250–262, sep 2005.
- [27] M. Manni, A. Ben Yehuda, Y. Klein, B. Lukic, A. Kingston, A. Rack, S. Shwartz, and N. Viganò, "Synchrotron-based X-ray Fluorescence Ghost Imaging," *Optics Letters*, vol. 48, no. 23, pp. 6271–6274, 2023.
- [28] M. Tancik, P. Srinivasan, B. Mildenhall, S. Fridovich-Keil, N. Raghavan, U. Singhal, R. Ramamoorthi, J. Barron, and R. Ng, "Fourier Features Let Networks Learn High Frequency Functions in Low Dimensional Domains," in *Advances in Neural Information Processing Systems*, H. Larochelle, M. Ranzato, R. Hadsell, M. F. Balcan, and H. Lin, Eds., vol. 33. Curran Associates, Inc., 2020, pp. 7537–7547.
- [29] D. P. Kingma and J. L. Ba, "Adam: A method for stochastic optimization," in *3rd International Conference on Learning Representations, ICLR 2015 - Conference Track Proceedings*, Y. Bengio and Y. LeCun, Eds., 2015.
- [30] <https://doi.org/10.5281/zenodo.7828494>.
- [31] D. S. Rigie and P. J. La Rivière, "Joint reconstruction of multi-channel, spectral CT data via constrained total nuclear variation minimization," *Physics in Medicine and Biology*, vol. 60, no. 5, pp. 1741–62, 2015.
- [32] T. Schoonjans, A. Brunetti, B. Golosio, M. Sanchez del Rio, V. A. Solé, C. Ferrero, and L. Vincze, "The xraylib library for X-ray–matter interactions. Recent developments," *Spectrochimica Acta Part B: Atomic Spectroscopy*, vol. 66, no. 11–12, pp. 776–784, nov 2011.